



Microwave-assisted optimization of platinum-nickel nanoalloys for catalytic water treatment



Hanyu Ma, Haitao Wang, Chongzheng Na*

Department of Civil and Environmental Engineering and Earth Sciences, University of Notre Dame, 156 Fitzpatrick Hall, Notre Dame, IN 46556, United States

ARTICLE INFO

Article history:

Received 12 May 2014

Received in revised form 3 July 2014

Accepted 29 July 2014

Available online 7 August 2014

Keywords:

Industrial wastewater treatment

Nitroaromatic reduction

Bimetallic alloy

Nano catalyst

Noble metal catalyst

ABSTRACT

Blending noble metal catalysts with inexpensive transition metals can reduce material cost in catalytic water treatment by improving the catalytic reactivity. An important challenge is, however, to synthesize a series of alloy nanoparticles with varied compositions so that the screening of catalytic reactivity can be performed rapidly for a contaminant of interest. Here, we report a facile approach for the rapid synthesis of bimetallic nanoalloys using cycle-controlled microwave-assisted polyol reduction, with an option of fixing the nanoalloys directly on graphene supports in a one-pot operation. Using Pt and Ni as the model noble and promoter metals, we show that Pt/Ni nanoparticles with diameters ranging from 2.8 to 4 nm can be readily synthesized within minutes. The surface Ni percentage of the nanoparticles are varied from 0 to 100%, which serves as a model system for nanoalloy screening. Using the model contaminant *p*-nitrophenol, we further show that the reactivity-composition relationship has a classic volcano shape as the Sabatier principle predicts. The highest reactivity is found with a surface Ni percentage of approximately 50%.

© 2014 Elsevier B.V. All rights reserved.

1. Introduction

Nanoparticles made of noble metals such as platinum (Pt), palladium (Pd), and gold (Au) have attracted increasing attention as catalysts for degrading organic and inorganic contaminants found in water and wastewater [1–7]. Compared to conventional treatment techniques, the use of catalysts can shorten treatment time, target recalcitrant compounds, and selectively transform wastes into valuable products. These attributes are particularly attractive as water reuse and resource recovery become increasingly incorporated into treatment practices [8,9]. An important challenge is, however, to reduce the high cost associated with the initial investment and subsequent replenishment of catalysts.

An effective strategy for reducing the cost of catalytic water treatment is to improve the reactivity of noble metal catalysts by blending them with promoter metals, forming bimetallic alloys. According to the classical Sabatier principle [10], an improved reactivity can be obtained by optimizing the reactant-catalyst interaction. For example, platinum is one of the best noble metals for catalyzing the degradation of environmental contaminants such as the reduction of *p*-nitrophenol (PNP) [1,11]. The reactivity of

Pt can be further improved by blending with 3d transition metals such as copper (Cu) and nickel (Ni) [12–14], which are ineffective catalysts themselves. The improved reactivity after blending is attributable to the reduction of reactant-catalyst affinity through electronic (lowering the *d*-band center) and geometric (reducing bond distances) effects [15].

An important parameter that controls the reactivity of a bimetallic alloy catalyst is the blending ratio between the noble and transition metals, with the highest reactivity often found at an intermediate blending ratio (not necessarily 1:1). The relationship between reactivity and blending ratio is often revealed as a volcano curve with an apex indicating an optimized energy for reactant adsorption [16–20]. The compositional dependence of reactivity has been the basis of selecting effective catalysts for important reactions such as the oxygen reduction reaction [21,22], the methanol oxidation reaction [23,24], and the hydrolysis of ammonia borane [25,26]. In comparison, only limited efforts have been given to environmentally relevant reactions such as the PNP reduction. Stevenson, Henkelman, and colleagues investigated the reactivity of Pt/Cu alloy nanoparticles (aka. nanoalloys) at a 1:1 molar ratio; however, the ratio between Pt and Cu was not varied [14]. Pal and colleagues studied the reactivity of Pt/Ni nanoalloys with Pt:Ni ratios of 36:64, 20:80, and 4:96 [12,27]. However, the highest reactivity was found at the extreme ratio of 4:96 in their systems, inconsistent with the optimal intermediate blending ratios found for other reactions (Pt:Ni = 1:1 to 3:1) [24,28,29].

* Corresponding author. Tel.: +1 574 631 5164.

E-mail address: chongzheng.na@gmail.com (C. Na).

To examine the compositional dependence of the catalytic reactivity of Pt nanoalloys in the PNP reduction, we synthesized Pt/Ni nanoparticles with varied surface compositions using a cycle-controlled microwave-assisted polyol reduction method. PNP is a Clean Water Act priority pollutant with an acceptable daily intake (ADI) of 0.32 mg per day over a month [30,31]. In comparison, the toxicity of reduced product *p*-aminophenol (PAP) is negligible with a ADI of 4.55 mg per day over a lifetime [32]. We selected Ni instead of Cu because Ni was expected to be more effective in weakening the adsorption energy of Pt with PNP [33,34], thereby providing a wider range for optimization. Through a quantitative volcano curve, we found the highest reactivity associated with a surface composition of near equimolar Pt and Ni. Furthermore, our synthesis method permitted the direct fixation of nanoalloys on microwave-absorbing supports such as graphene sheets, for the benefit of an extended service life. Our results suggest that blending noble metals with proper inexpensive promoters is a potentially feasible solution for reducing the cost of catalytic water treatment. The microwave-assisted method provides a facile and green approach [35,36] for nanoalloy synthesis so that the rapid optimization can be potentially performed for other targeted contaminants as well.

2. Experimental

All chemicals of reagent grade were purchased from Sigma Aldrich except otherwise specified. Deionized (DI) water was generated on site using a Millipore system.

2.1. Synthesis of Pt nanoparticles and Pt/Ni nanoalloys

Stock solutions of platinum chloride (PtCl_2 ; 1.40 mM) and nickel chloride (NiCl_2 ; 1.43 mM) were prepared by dissolving 5.6 mg PtCl_2 and 5.1 mg $\text{NiCl}_2 \cdot 6\text{H}_2\text{O}$ in 15 mL diethyleneglycol (DEG), respectively, under vigorous stirring for 1 hour. Unsupported Pt/Ni nanoalloys were synthesized in 6 steps. First, 1 mL PtCl_2 and 1 mL NiCl_2 stock solutions were added to 5.5 mL DEG in a 20 mL scintillation vial and mixed by magnetic stirring for 15 minutes. Second, the vial was placed in a commercial microwave oven (R-209KK, Sharp Electronics Corp., Mahwan, New Jersey; 800 W, 2.45 GHz). Microwave radiation was administered in 1–8 cycles, each of which consisted of a 50-second “on” segment at the maximum power followed by a 30-second “off” segment. Third, the vial was taken out of the microwave oven and cooled in air to room temperature. Fourth, the reaction mixture was then centrifuged at $17,000 \times g$ for 5 min to recover nanoalloys. The recovered nanoalloys were washed with 20 vol% acetone aqueous solution and then centrifuged for three times. Fifth, the cleaned nanoalloys were placed in a fume hood to evaporate residual water and acetone. The recovery efficiency of centrifugation and wash process was estimated at 75% using a known amount of Pt nanoparticles. Last, dried nanoalloys were dispersed in 7.5 mL DI water under sonication for 25 min. To make Pt nanoparticles, only the PtCl_2 solution was used in the first step.

2.2. Synthesis of graphene-supported Pt/Ni nanoalloys

Graphene oxide (GO) was prepared by the oxidative exfoliation of natural graphite (325 mesh, 96%, Alfa Aesar) according to the modified Hummers’ method [37]. Briefly, 1 g graphite and 1 g sodium nitrate (NaNO_3) were added into 46 mL 98% sulfuric acid (H_2SO_4) in an ice bath under stirring. Six grams of potassium permanganate (KMnO_4) was slowly added to the mixture and stirred for 15 minutes. The mixture was then heated at 35°C and stirred vigorously for 30 min into a thick paste. Ninety milliliters of DI water was slowly introduced to the mixture to sustain the reaction for another 40 minutes at 98°C . Finally, 280 mL DI water was added to dilute the mixture and 5 mL 30% hydrogen peroxide (H_2O_2) was added to the mixture to terminate the reaction. GO was centrifuged

and washed repeatedly with DI water to remove the remaining oxidizing reagents and salt products. The precipitate was freeze-dried (Labconco Freezone 4.5) into a powder for storage.

The stock solution of 290 mg L^{-1} GO was prepared by dispersing 15 mg GO powder in 52 mL DEG under sonication for 30 min. Graphene-supported Pt (G-Pt) nanoparticles and graphene-supported Pt/Ni (G-Pt/Ni) nanoalloys were synthesized following the 6-step procedure described for unsupported nanoalloys with the exception that DEG was replaced by the same volume of a stock solution of GO and DEG mixture.

2.3. Material characterization

Samples of supported and unsupported nanoalloys were characterized using a series of analytical techniques. Morphologies and sizes of nanoparticles and nanoalloys were examined using transmission electron microscopy (TEM; FEI Titan 80-300). High resolution TEM (HRTEM) images were taken to elucidate shape and crystallinity. Chemical composition was determined directly using energy-dispersive X-ray spectroscopy (EDX; Quantax 200) and X-ray fluorescence spectroscopy (XRF, Orbis Micro-XRF Analyzer) and indirectly using ion-coupled plasma optical emission spectroscopy (ICP-OES, Perkin Elmer Optima 2000) after acid digestion. For the XRF analysis, samples were drop-casted on silicon chips (University Wafer, Boston, Massachusetts) and dried in air. For the ICP-OES analysis, 1 mL aqueous solution was air-dried in a quartz vial, mixed with 1 mL aqua regia ($\text{HCl}:\text{HNO}_3 = 3:1$), heated to 80°C , and digested for 4 h. The solution was diluted for 5 times and filtered through a $0.45\text{ }\mu\text{m}$ nylon membrane before introducing into the ICP-OES instrument. The yields of Pt and Ni were computed from the changes of Pt and Ni concentrations obtained from ICP-OES measurements before and after microwave irradiation. Molecular models of nanoalloys were created using CrystalMarker[®].

2.4. Catalytic reduction of *p*-nitrophenol

To measure the catalytic reactivity of supported and unsupported nanoalloys, 1 mL aqueous solution was mixed with 32 mM sodium borohydride (NaBH_4) at a 1:1 volumetric ratio. To start the reduction reaction, $10\text{ }\mu\text{L}$ of 20 mM PNP was added into a 2 mL catalyst- NaBH_4 mixture in a standard UV/vis quartz cuvette. The progress of the reduction was monitored using a UV/vis

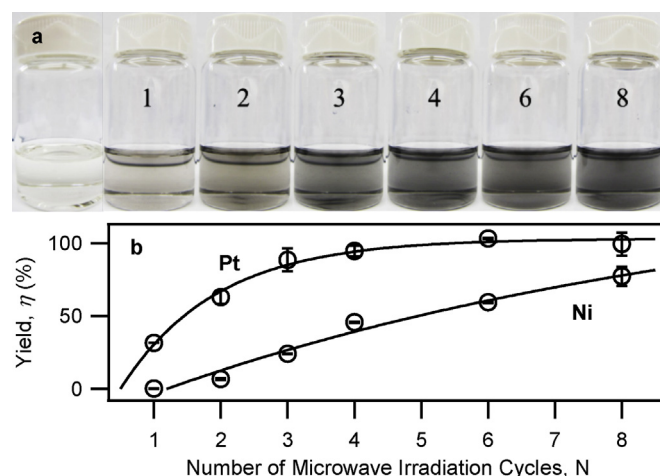


Fig. 1. Variation of Pt/Ni nanoalloy composition with the number of microwave irradiation cycles (1 cycle = 50 s on and then 30 s off). (a) Digital photographs of the synthesis solution before and after microwave irradiation (marked with the number of irradiation cycles). (b) Conversion of Pt and Ni from solution to particle measured by ICP-OES after acid digestion. The curves are exponential fits to show the trends of Pt and Ni yields.

spectrophotometer (Agilent Cary 300). The reactive solution was stirred the whole time using a glass rod. The absorption of light from 220 to 520 nm by the reactive solution was recorded once every minute. Before each experiment, the baseline was measured using a solution consisting of 1 mL of the corresponding material solution and 1 mL of 32 mM NaBH₄ without PNP. The baseline was subtracted from the absorption spectra of the reactive solution for the quantification of PNP. The PNP concentration was converted from absorbance using a calibration curve obtained with PNP solutions of known concentrations. To test the reactivity of the catalysts in repeated use, the reaction solution was centrifuged at 17,000 × *g* for 5 min to recover the catalysts. The catalysts were re-dispersed in 1 mL water by 5 min sonication and the catalytic activity was tested as described above.

3. Results

Metal nanoparticles formed by irradiating a synthesis solution containing Pt²⁺, Ni²⁺, and diethylene glycol with microwaves are

shown in Fig. 1. As the number of irradiation cycles increases from *N* = 1 to 4 (1 cycle = 50 s on and 30 s off), the colour of the synthesis solution becomes darker (Fig. 1a), indicating a continuous increase of the total volume of metal nanoparticles. Indeed, the ICP-OES analysis shows increasing amounts of Pt and Ni found in the nanoparticles from cycle 1 to 4 after they are completely digested using aqua regia (Fig. 1b). Interestingly, nanoparticles formed by a single cycle of microwave irradiation (*N* = 1) contain only Pt and Pt is always favored over Ni by the polyol reduction reaction during synthesis. The further increase of *N* above 4 exhausts the supply of Pt with the additional reduction of Ni alone.

Representative nanoparticles formed with *N* = 1, 3, and 6 are further examined under high-resolution TEM. As shown in Fig. 2, the nanoparticles are single crystals with truncated octahedral shapes that have 8 {111} faces and 6 {100} faces. Their single crystallinity is confirmed by the discrete electron diffraction patterns obtained from the Fast Fourier transform of the micrographs. For particles shown in Fig. 2a and b, the patterns are consistent with the {111} and {002} reflections of the cubic close-packed structures of Pt and

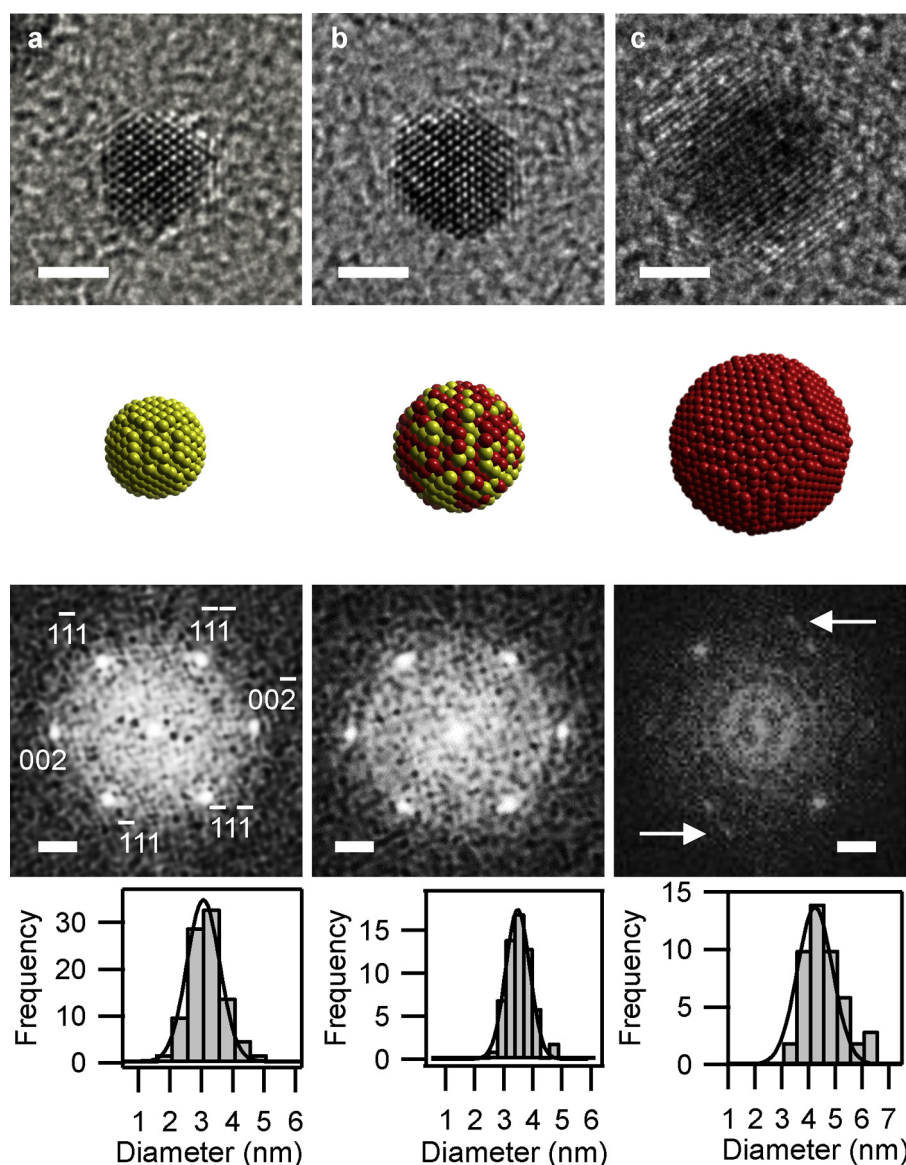


Fig. 2. Transmission electron micrographs (TEMs) of representative Pt/Ni nanoparticles synthesized under (a) 1, (b) 3, and (c) 6 cycles of microwave irradiation (1 cycle = 50 s on and 30 s off). Molecular models (truncated octahedrons) representing the nanoparticles, electron diffraction patterns obtained from Fourier transform (FFT), and histograms of nanoparticle diameters are shown underneath the TEMs. In the molecular models, Pt and Ni are colored in gold and red, respectively. In the FFT images, most of diffraction spots are generated by the {111} and {002} reflections of Pt or Pt/Ni lattices with the exception that the two spots marked by the arrows in c are the {111} reflection of Ni. Scale bars: TEM, 2 nm; FFT, 2 nm⁻¹. (For interpretation of the color information in this figure legend, the reader is referred to the web version of the article.)

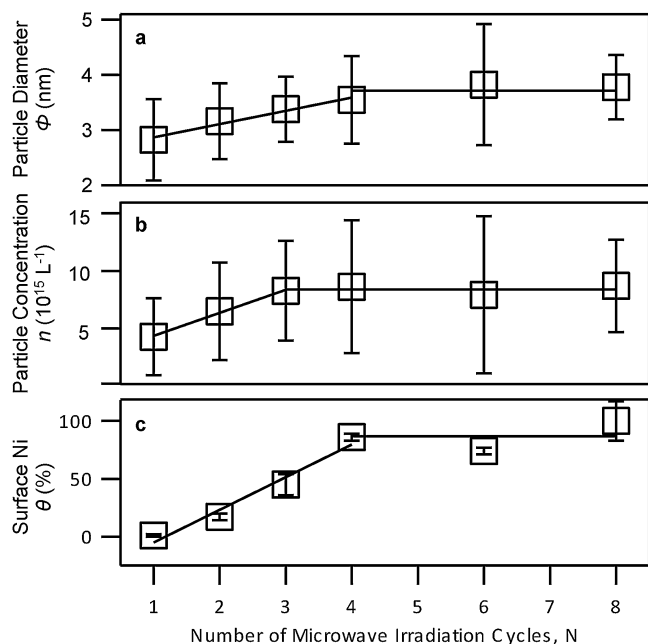


Fig. 3. Changes of (a) particle diameter, (b) particle number concentration, and (c) surface Ni percentage with the number of microwave irradiation cycles (1 cycle = 50 s on and then 30 s off). The error bars mark the standard deviations of Gaussian distributions. The lines are linear fits for low N and averages for high N , respectively.

Pt/Ni viewed in the [110] direction [38]. For the particle shown in Fig. 2c, two additional diffraction spots are visible, which are attributable to the {111} reflection of Ni. This is consistent with the fact that Pt is being depleted after 4 cycles of irradiation and a Ni-rich coating is formed with further irradiation (Fig. 1b). In addition to the continued variation of composition, the particle diameter also increases with increasing N , as shown by the diameter histograms.

Changes of particle diameter ϕ , particle number concentration n , and surface Ni percentage θ with increasing N are presented in Fig. 3. Measurements of ϕ made under TEM show that ϕ is normally distributed (Fig. 2). The mean value of ϕ increases linearly from 2.8 to ca. 4 nm as N increases from 1 to 4 and then plateaus as Pt^{2+} is depleted (Fig. 3a). n is computed from the initial molar concentrations of Pt^{2+} and Ni^{2+} ($C_{\text{Pt}} = C_{\text{Ni}} = 0.19 \text{ M}$), their yields (η_{Pt} and η_{Ni}), and the atomic volumes of Pt and Ni atoms in crystals ($v_{\text{Pt}} = 0.0151 \text{ nm}^3$ and $v_{\text{Ni}} = 0.0109 \text{ nm}^3$, which are calculated with their lattice parameters [39]):

$$n = \frac{6 (C_{\text{Pt}} \eta_{\text{Pt}}^N v_{\text{Pt}} + C_{\text{Ni}} \eta_{\text{Ni}}^N v_{\text{Ni}}) N_A}{\pi \phi^3} \quad (1)$$

where $N_A = 6.02 \times 10^{23}$ is Avogadro's number. n first increases linearly from $N=1$ to 3 as the nucleation process continues, after which n becomes stable (Fig. 4b). Similarly, θ increases linearly from $N=1$ to 4 and plateaus afterwards (Fig. 4c). Here, θ is computed as follows:

$$\theta = \frac{C_{\text{Ni}} (\eta_{\text{Ni}}^N - \eta_{\text{Ni}}^{N-1})}{C_{\text{Ni}} (\eta_{\text{Ni}}^N - \eta_{\text{Ni}}^{N-1}) + C_{\text{Pt}} (\eta_{\text{Pt}}^N - \eta_{\text{Pt}}^{N-1})} \quad (2)$$

For $N=1$, $\eta_{\text{Ni}}^0 = 0$. The values of θ are confirmed by EDX and XRF measurements (Figure S1).

The catalytic reactivity of Pt/Ni nanoparticles is evaluated using the model reaction of PNP reduction by sodium borohydride [40]. With an excess amount of borohydride, PNP is reduced to PAP in the presence of noble metal catalysts. We selected borohydride as the reducing agent for two reasons. First, the use of borohydride allows

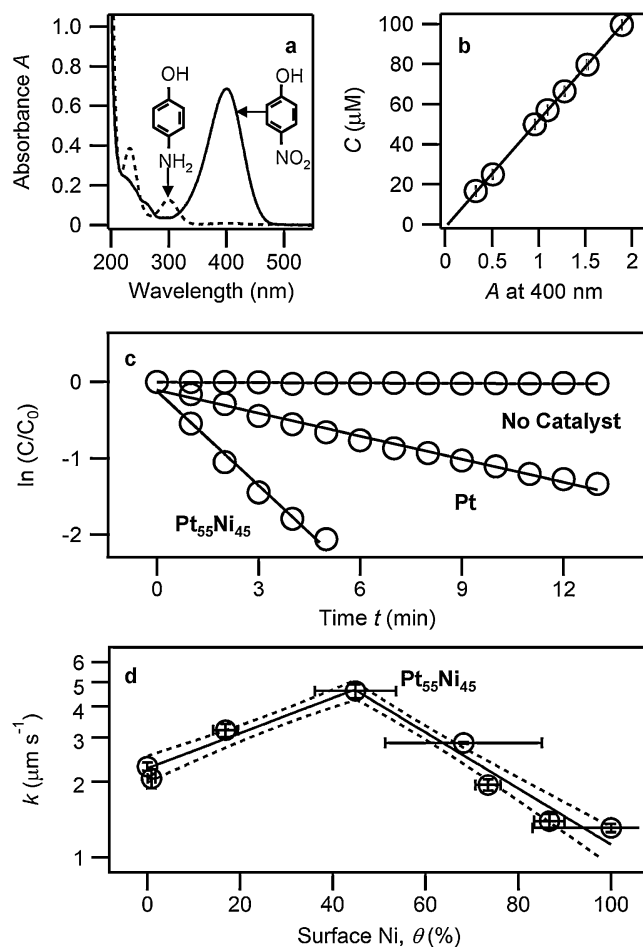


Fig. 4. Catalytic reduction of *p*-nitrophenol (PNP) by Pt/Ni nanoalloys. (a) Absorption spectra of PNP and the reduction product *p*-aminophenol (PAP). (b) Linear relationship between the PNP molar concentration and the absorbance at 400 nm. (c) Pseudo-first order kinetics of the PNP reduction. (d) Volcano plot of the normalized rate constant k and surface Ni percentage θ . The solid lines are exponential fits and the dashed lines bracket the 68.3% confidence interval.

us to compare the reactivity of Pt/Ni nanoalloys with other catalysts reported in the literature, which has been characterized almost exclusively using borohydride [12,14,27]. Second, borohydride has been previously proposed for recovering precious and heavy metals from wastewater [41]. For example, patents [42,43] and commercial available products [44,45] exist for removing copper from circuit-printing wastewater and nickel from plating wastewater.

As shown in Fig. 4a, PNP absorbs visible light strongly at 400 nm [46] whereas PAP absorbs little light from 325 to 600 nm [47]; therefore, the kinetics of PNP reduction can be quantified the concentration of residual PNP, C , by measuring the absorbance A at 400 nm following Beer's law: $C = \epsilon b A^{-1}$, where ϵ is the molar absorptivity of PNP and b is the path length ($b = 1 \text{ cm}$), as shown in Fig. 4b. As shown in Fig. 4c, the PNP reduction follows the pseudo-first order rate law in the presence of both Pt and Pt/Ni nanoparticles, which is in great contrast of the negligible reduction when both of them are absent:

$$\ln \frac{C}{C_0} = -k_1 t \quad (3)$$

where C_0 is the initial PNP concentration, t is the reaction time, and k_1 is the pseudo-first order rate constant. To remove the influence from the increase of catalyst surface area as the nanoparticle size and concentration increase, we further normalize k_1 to the surface

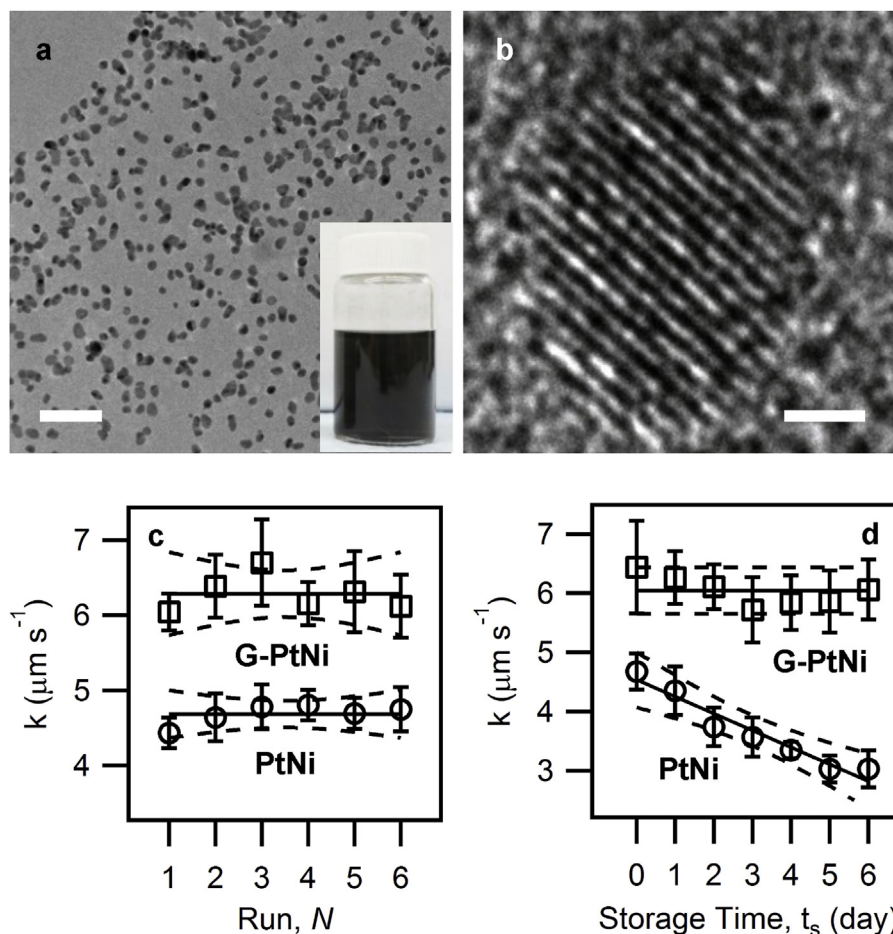


Fig. 5. Extended service lifetime of Pt/Ni nanoalloys on graphene support. (a, b) Transmission electron micrographs of single-crystalline Pt/Ni anchored on graphene (inset: digital photograph). Scale bars: a, 50 nm; b, 1 nm. (c) Comparison of catalytic rate constants for six consecutive runs. (d) Comparison of catalytic rate constants after storage.

area per unit volume (k) to compare the catalytic activity of Pt/Ni nanoalloys with different surface compositions:

$$k = k_1 \frac{6}{\pi \phi^3 n} \quad (4)$$

After normalization, a volcano-shaped relation appears between k and θ , as shown in Fig. 4d, suggesting that there is an optimal Pt/Ni blending ratio corresponding to the highest catalytic reactivity at $\theta = 44(\pm 7)\%$. It is worth noting that Pt/Ni nanoalloys outperform both pure Pt and Ni catalysts (i.e., $\theta = 0$ and 100, respectively), in agreement with findings by Pal and colleagues [12,24] although the optimal composition found by us contains much less Ni than theirs. The reaction rates measured for Pt nanoparticles and nanoalloys with complete Ni shells are comparable to the rates for pure Pt or Ni nanoparticles measured by other researchers [12,48–50].

The near-equimolar Pt/Ni nanoalloys can be readily fixed on graphene sheets to prevent nanoparticle aggregation and facilitate particle recycling during treatment operation. This is done by adding single-layer graphene oxide sheets into the synthesis solution, which was reduced by DEG to graphene sheets [23,51]. As shown in Fig. 5a and b, the nanoalloys are well spread on graphene sheets as single crystals. The ICP-OES analysis shows that the nanoalloys on graphene have the same composition as the unsupported nanoalloys with a surface Pt:Ni ratio of 1:1 (Pt:Ni = 76:24 overall). The catalytic activities of both the Pt/Ni nanoparticles and the supported alloy (G-PtNi) keep unchanged in six runs as shown in Fig. 5c, indicating the catalysts are stable under the reaction conditions. However, G-PtNi shows a much longer service life than its

unsupported counterpart, thanks to the resistance to aggregation provided by graphene sheets, as shown in Fig. 5d.

4. Discussion

Results described in the previous section have provided valuable insights for the mechanism of Pt/Ni alloy formation and the mechanism underlying their improved reactivity. These mechanisms are discussed in this section.

4.1. Mechanism of Pt/Ni nanoalloy formation under microwave irradiation

The compositional change of Pt/Ni nanoalloy with increasing the number of irradiation cycles suggests a complex mechanism of formation. Three steps can be deduced from the experimental observations, including (1) the nucleation of a Pt core, (2) the growth of Pt/Ni shells, and (3) the termination with a Ni shell, as shown in Fig. 6.

The formation of a Pt core is attributable to its positive standard reduction potential, which is $E^\circ(\text{Pt}^{2+}/\text{Pt}) = 1.2\text{ V}$ compared to $E^\circ(\text{Ni}^{2+}/\text{Ni}) = -0.27\text{ V}$ [39]. In our synthesis, DEG is used as both solvent and reducing agent, which first dehydrates to acetaldehyde and is then oxidized to diacetyl [52,53]. The positive value of $E^\circ(\text{Pt}^{2+}/\text{Pt})$ ensures that the reaction between Pt^{2+} and DEG proceed readily. In contrast, the negative value of $E^\circ(\text{Ni}^{2+}/\text{Ni})$ makes the reaction of Ni^{2+} and DEG difficult. Our control experiment performed with Ni^{2+} and DEG in the absence of Pt^{2+} showed

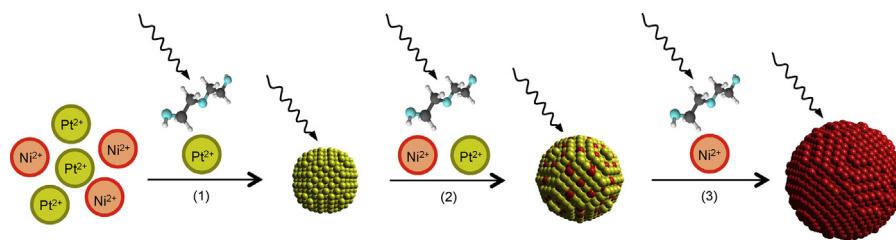


Fig. 6. Mechanism of Pt/Ni nanoalloy formation under microwave irradiation.

no nanoparticle formation up to 4 cycles of microwave irradiation, suggesting that DEG's potential is insufficient to reduce Ni^{2+} directly at the synthesis temperature created by the dielectric heating of DEG [54]. When the good microwave absorber GO is present [55], the nucleation of nanoparticles occurs on GO where it has a greater temperature than the solution.

After Pt cores are formed, they become catalysts with surfaces to facilitate the reduction of Ni^{2+} by DEG [56]. The reduction reaction is further enhanced as Pt absorbs microwaves by forming eddy currents [57,58], thereby achieving a temperature above the DEG solution [59]. Under such conditions, both Pt and Ni are added as nanoparticles grow in size although Pt is still favoured over Ni. Once Pt^{2+} is depleted, only Ni is coated on the outside of the nanoparticles.

The use of mild polyol reductants such as DEG is critical for producing the layer-by-layer compositional change of the nanoparticles. When a strong reductant such as hydrazine is used ($E^\circ(\text{N}_2/\text{N}_2\text{H}_4) = -1.16 \text{ V}$ [60]), the composition of an added layer is controlled by the relative concentration of Pt^{2+} and Ni^{2+} in solution because hydrazine readily reduces both cations. For example, when hydrazine reacts with an aqueous solution containing PtCl_6^{2-} and Ni^{2+} in a molar ratio of 4:96 [12,27], we can expect Ni^{2+} is consumed much faster than PtCl_6^{2-} . Consequently, at the end of the reaction, the surface Pt:Ni ratio of nanoparticles can be much higher than 4:96. This may reconcile the different optimal Pt:Ni compositions found by us and by Pal and colleagues [12,27].

4.2. Mechanism of the improved catalytic reactivity of Pt/Ni nanoalloys

According to the classic Langmuir–Hinshelwood model [40], the reduction of PNP by borohydride over a metal catalyst occurs after both reactants are adsorbed onto the metal surface. Although the transformation of PNP to PAP is a multi-step reaction, the rate limiting step is the adsorption of PNP under the alkaline condition with excess borohydride [61]. The potential for an inadequate adsorption of BH_4^- is not of concern because borohydride is always in excess. As shown in Fig. 4d, two exponential functions are found on both sides of the optimal Pt/Ni composition (i.e., $\theta = 44\%$), revealing the limiting conditions with overly strong PNP adsorptions by Pt on the left and by Ni on the right [62].

As a 5d transition metal, Pt is located at the lower right of the transition-metal block in the periodic table; therefore, the interaction of Pt with PNP is already lower than most of the other transition metals according to the d-band theory [34]. To further lower the interaction energy, Pt can be doped with 3d transition metals, which reduces the adsorption energy of the catalyst by affecting the electronic structure of Pt (the ligand effect) and the lattice structure at the surface (the strain effect) [33,63]. In particular, the strain effect is related to the reduction of interatomic distance. In our experiments, the reduction of interatomic distance upon Ni doping is evident from the reduction of lattice spacing. As shown in Fig. 7, d_{111} measured from the FFT images in Fig. 2 transitions from the value for Pt toward that for Ni as θ increases

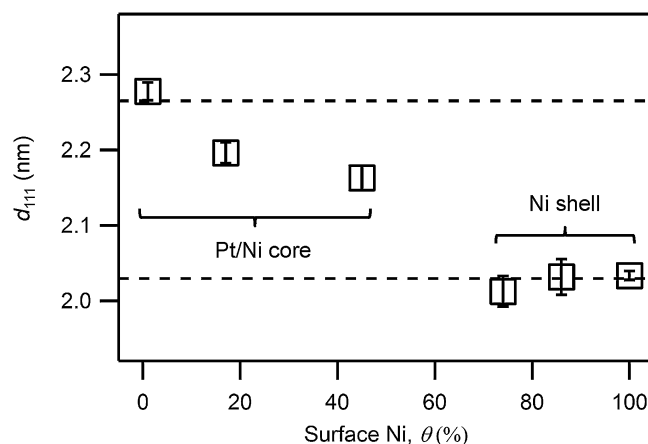


Fig. 7. Reduction of the lattice spacing between $\{111\}$ planes, d_{111} , with the increase of surface Ni percentage θ .

[38]. The Pt/Ni nanoalloy having the best performance is associated with an intermediate d_{111} value, presumably corresponding to the largest change of electronic configuration with the change of lattice structure.

It is worth noting that the rationalization presented above does not take into account the change of the Fermi level of a metal nanoparticle as its size decreases. When the nanoparticle accepts an excess electron density of δ from an adsorbate (e.g., borohydride in the PNP reduction; $\delta \approx 0.3$), the nanoparticle's Fermi level E_F is increased under an inverse relationship with the nanoparticle size [56]: $\Delta E_F = 8E_F\delta r\phi^{-1}$, where r is the atomic radius ($r = 0.14 \text{ nm}$ for Pt [39]). The increase of E_F reduces the adsorption energy over the metal surface and thus improves reactivity. With $\phi = 2.8\text{--}4 \text{ nm}$ as we have in our experiments, $\Delta E_F/E_F$ stabilizes in the range of 10–14%; therefore, the effect of Fermi-level increase is insignificant. For nanoparticles with a diameter of 1 nm [14,64], $\Delta E_F/E_F$ can be as large as 40%; therefore, the optimal composition may change as the size of nanoparticles varies.

5. Conclusions

We have successfully synthesized suspended Pt/Ni nanoalloys using a cycle-controlled microwave-assisted polyol reduction method. This one-pot method creates nanoparticles with a range of surface compositions without much change of the particle size. The varied surface compositions permit the rapid determination of the optimal Pt/Ni composition to be used as an effective nanoalloy for reducing the model water contaminant *p*-nitrophenol. The adoption of the facile synthesis method in catalyst designs may permit the rapid screening of nanoalloys for other water contaminants.

Acknowledgements

This work was mainly supported by the USDOE Office of Nuclear Energy's Nuclear Energy University Programs, the U.S. National

Science Foundation's Environmental Engineering Program, and the University of Notre Dame Sustainable Energy Initiative. H.M. thanks support from the Bayer Predoctoral Research Fellowship provided by the Notre Dame Center for Environmental Science and Technology.

Appendix A. Supplementary data

Supplementary data associated with this article can be found, in the online version, at <http://dx.doi.org/10.1016/j.apcatb.2014.07.062>.

References

- [1] S. Wunder, F. Polzer, Y. Lu, Y. Mei, M. Ballauff, *J. Phys. Chem. C* 114 (2010) 8814–8820.
- [2] T. Pradeep, Anshup, *Thin Solid Films* 517 (2009) 6441–6478.
- [3] J. Liu, J.K. Choe, Z. Sasnow, C.J. Werth, T.J. Strathmann, *Water Res.* 47 (2013) 91–101.
- [4] H. Wang, Z. Dong, C. Na, *ACS Sustainable Chem. Eng.* 1 (2013) 746–752.
- [5] S. De Corte, T. Sabbe, T. Hennebel, L. Vanhaecke, B. De Gussemme, W. Verstraete, N. Boon, *Water Res.* 46 (2012) 2718–2726.
- [6] H. Wang, H. Ma, W. Zheng, D. An, C. Na, *ACS Appl. Mater. Interf.* 6 (2014) 9426–9434.
- [7] B.P. Chaplin, M. Reinhard, W.F. Schneider, C. Schüth, J.R. Shapley, T.J. Strathmann, C.J. Werth, *Environ. Sci. Technol.* 46 (2012) 3655–3670.
- [8] N. Wigginton, J. Yeston, D. Malakoff, *Science* 337 (2012) 662–663.
- [9] J.G. Hering, T.D. Waite, R.G. Luthy, J.E. Drewes, D.L. Sedlak, *Environ. Sci. Technol.* 47 (2013) 10721–10726.
- [10] P. Sabatier, *Berichte der deutschen chemischen Gesellschaft* 44 (1911) 1984–2001.
- [11] J. Kaiser, L. Leppert, H. Welz, F. Polzer, S. Wunder, N. Wanderka, M. Albrecht, T. Lunkenbein, J. Breu, S. Kummel, Y. Lu, M. Ballauff, *Phys. Chem. Chem. Phys.* 14 (2012) 6487–6495.
- [12] S.K. Ghosh, M. Mandal, S. Kundu, S. Nath, T. Pal, *Appl. Catal., A* 268 (2004) 61–66.
- [13] R. Liu, Q. Zhao, Y. Li, G. Zhang, F. Zhang, X. Fan, *J. Nanomater.* 2013 (2013) 7.
- [14] Z.D. Pozun, S.E. Rodenbusch, E. Keller, K. Tran, W. Tang, K.J. Stevenson, G. Henkelman, *J. Phys. Chem. C* 117 (2013) 7598–7604.
- [15] K. Jayasayee, J.A.R.V. Veen, T.G. Manivasagam, S. Celebi, E.J.M. Hensen, F.A. de Bruijn, *Appl. Catal., B* 111–112 (2012) 515–526.
- [16] H. Toulhoat, P. Raybaud, S. Kasztelan, G. Kresse, J. Hafner, *Catal. Today* 50 (1999) 629–636.
- [17] R.R. Chianelli, G. Berhault, P. Raybaud, S. Kasztelan, J. Hafner, H. Toulhoat, *Appl. Catal., A* 227 (2002) 83–96.
- [18] K. Tedsree, C.W.A. Chan, S. Jones, Q.A. Cuan, W.K. Li, X.Q. Gong, S.C.E. Tsang, *Science* 332 (2011) 224–228.
- [19] R.I. Masel, *Chemical Kinetics and Catalysis*, John Wiley & Sons, New York, NY, 2001.
- [20] V.R. Stamenkovic, B. Fowler, B.S. Mun, G. Wang, P.N. Ross, C.A. Lucas, N.M. Marković, *Science* 315 (2007) 493–497.
- [21] T. Toda, H. Igarashi, H. Uchida, M. Watanabe, *J. Electrochem. Soc.* 146 (1999) 3750–3756.
- [22] M.H. Shao, K. Sasaki, R.R. Adzic, *J. Am. Chem. Soc.* 128 (2006) 3526–3527.
- [23] Y. Liu, M.F. Chi, V. Mazumder, K.L. More, S. Soled, J.D. Henao, S.H. Sun, *Chem. Mater.* 23 (2011) 4199–4203.
- [24] Y. Hu, P. Wu, Y. Yin, H. Zhang, C. Cai, *Appl. Catal., B* 111 (2012) 208–217.
- [25] D.H. Sun, V. Mazumder, O. Metin, S.H. Sun, *ACS Nano* 5 (2011) 6458–6464.
- [26] J.M. Yan, X.B. Zhang, S. Han, H. Shioyama, Q. Xu, *J. Power Sources* 194 (2009) 478–481.
- [27] M. Mandal, S. Kundu, S.K. Ghosh, T.K. Sau, S.M. Yusuf, T. Pal, *J. Colloid Interface Sci.* 265 (2003) 23–28.
- [28] H. Yang, W. Vogel, C. Lamy, N. Alonso-Vante, *J. Phys. Chem. B* 108 (2004) 11024–11034.
- [29] S.I. Choi, S.U. Lee, W.Y. Kim, R. Choi, K. Hong, K.M. Nam, S.W. Han, J.T. Park, *ACS Appl. Mater. Interfaces* 4 (2012) 6228–6234.
- [30] United States Environmental Protection Agency, Clean Water Act Priority Pollutant List, 1982, pp. Code of Federal Regulations 40 CFR 423 Appendix A.
- [31] United States Public Health Service, Toxicological profile for nitrophenols: 2-nitrophenol 4-nitrophenol, 1992.
- [32] United States Environmental Protection Agency, Health and Environmental Effects Profile for Aminophenols, 1985.
- [33] J.R. Kitchin, J.K. Norskov, M.A. Barteau, J.G. Chen, *J. Chem. Phys.* 120 (2004) 10240–10246.
- [34] B. Hammer, J.K. Norskov, Theoretical surface science and catalysis – Calculations and concepts, in: B.C. Gates, H. Knozinger (Eds.), *Advances in Catalysis*, Vol 45: Impact of Surface Science on Catalysis, Elsevier Academic Press Inc, San Diego, 2000, pp. 71–129.
- [35] M. Nuchter, B. Ondruschka, W. Bonrath, A. Gum, *Green Chem.* 6 (2004) 128–141.
- [36] J. Kou, C. Bennett-Stamper, R.S. Varma, *ACS Sustainable Chem Eng.* 1 (2013) 810–816.
- [37] W.S. Hummers, R.E. Offeman, *J. Am. Chem. Soc.* 80 (1958), 1339–1339.
- [38] R.W.G. Wyckoff, *Crystal Structures*, second ed., Interscience Publishers, New York, 1963.
- [39] D.R. Lide, *CRC Handbook of Chemistry and Physics*, CRC Press, New York, 2006.
- [40] P. Hervés, M. Pérez-Lorenzo, L.M. Liz-Marzán, J. Dzubiella, Y. Lu, M. Ballauff, *Chem. Soc. Rev.* 41 (2012) 5577–5587.
- [41] C. Gómez-Lahoz, F. García-Herruzo, J.M. Rodríguez-Maroto, J.J. Rodríguez, *Water Res.* 27 (1993) 985–992.
- [42] J.A. Ulman, W. Verstraeten, M.A. Cook, W. Verleye, L.J. Guilbault, Separating metals from waste water, US Patent: 5354478 A (1994).
- [43] C.L. Alexander, A.M. Mariniello, B.A. McBride, M.M. Cook, D.A. Dunn, Waste treatment of metal plating solutions, US Patent: USH1852 H (2000).
- [44] The Dow Chemical Company, VenMet™ Borohydride Solution, 2013.
- [45] Kemira Oyj, Sodium borohydride products, <http://www.kemira.com/en/industries-applications/Pages/sodium-borohydride.aspx>, June 29, 2014.
- [46] J. Liu, G. Qin, P. Raveendran, Y. Ikushima, Y. Ikushima, *Chem. Eur. J.* 12 (2006) 2131–2138.
- [47] D.M. Dotzauer, S. Bhattacharjee, Y. Wen, M.L. Bruening, *Langmuir* 25 (2009) 1865–1871.
- [48] Z. Jiang, J. Xie, D. Jiang, X. Wei, M. Chen, *CrystEngComm* 15 (2013) 560–569.
- [49] K. Esumi, R. Isono, T. Yoshimura, *Langmuir* 20 (2004) 237–243.
- [50] N. Sahiner, H. Ozay, O. Ozay, N. Aktas, *Appl. Catal., A* 385 (2010) 201–207.
- [51] P. Kundu, C. Nethravathi, P.A. Deshpande, M. Rajamathi, G. Madras, N. Ravishanker, *Chem. Mater.* 23 (2011) 2772–2780.
- [52] F. Fievet, J.P. Lagier, B. Blin, B. Beaudoin, M. Figlarz, *Solid State Ionics* 32–3 (1989) 198–205.
- [53] S.E. Skrabalak, B.J. Wiley, M. Kim, E.V. Formo, Y. Xia, *Nano Lett.* 8 (2008) 2077–2081.
- [54] Z.G. Wang, Y. Hu, W.L. Yang, M.J. Zhou, X. Hu, *Sensors* 12 (2012) 4860–4869.
- [55] A.V. Murugan, T. Muraliganth, A. Manthiram, *Chem. Mater.* 21 (2009) 5004–5006.
- [56] D.S. Li, S. Komarneni, *J. Am. Ceram. Soc.* 89 (2006) 1510–1517.
- [57] R. Roy, D. Agarwal, J.P. Chen, S. Gedevarishvili, *Nature* 399 (1999) 668–670.
- [58] N. Yoshikawa, *J. Microwave Power* 44 (2010) 4–13.
- [59] J. Obrzut, J.F. Douglas, O. Kirillov, F. Sharifi, J.A. Liddle, *Langmuir* (2013) 9010–9015.
- [60] K.N. Yu, D.J. Kim, H.S. Chung, H.Z. Liang, *Mater. Lett.* 57 (2003) 3992–3997.
- [61] A. Agrawal, P.G. Tratnyek, *Environ. Sci. Technol.* 30 (1995) 153–160.
- [62] J. Cheng, P. Hu, P. Ellis, S. French, G. Kelly, C.M. Lok, *J. Phys. Chem. C* 112 (2008) 1308–1311.
- [63] Y. Xu, A.V. Ruban, M. Mavrikakis, *J. Am. Chem. Soc.* 126 (2004) 4717–4725.
- [64] J.A. Johnson, J.J. Makis, K.A. Marvin, S.E. Rodenbusch, K.J. Stevenson, *J. Phys. Chem. C* 117 (2013) 22644–22651.